

Stabilization mechanism of molecular orbital crystals in IrTe₂

Tobias Ritschel¹[✉], Quirin Stahl¹, Maximilian Kusch¹, Jan Trinckauf², Gaston Garbarino³, Volodymyr Svitlyk^{3,4}, Mohamed Mezouar³, Junjie Yang⁵, Sang-Wook Cheong⁶ & Jochen Geck^{1,7}[✉]

Doped IrTe₂ is considered a platform for topological superconductivity and therefore receives currently a lot of interest. In addition, the superconductivity in these materials exists in close vicinity to electronic order and the formation of molecular orbital crystals, which we explore here by means of high-pressure single crystal x-ray diffraction in combination with density functional theory. Our crystallographic refinements provide detailed information about the structural evolution as a function of applied pressure up to 42 GPa. Using this structural information for density functional theory calculations, we show that the local multicenter bonding in IrTe₂ is driven by changes in the Ir-Te-Ir bond angle. When the electronic order sets in, this bond angle decreases drastically, leading to a stabilization of a multicenter molecular orbital bond. This unusual local mechanism of bond formation in an itinerant material provides a natural explanation for the different electronic orders in IrTe₂. It further illustrates the strong coupling of the electrons with the lattice and is most likely relevant for the superconductivity in this material.

¹Institute of Solid State and Materials Physics, TU Dresden, 01069 Dresden, Germany. ²Leibniz Institute for Solid State and Materials Research IFW Dresden, Helmholtzstr. 20, 01069 Dresden, Germany. ³European Synchrotron Radiation Facility, BP 220, F-38043 Grenoble, Cedex, France. ⁴Institute of Resource Ecology, Helmholtz-Zentrum Dresden-Rossendorf, 01314 Dresden, Germany. ⁵Department of Physics, New Jersey Institute of Technology, Newark, NJ 01702, USA. ⁶Rutgers Center for Emergent Materials and Department of Physics and Astronomy, Rutgers, The State University of New Jersey, 136 Frelinghuysen Road, Piscataway, NJ 08854-8019, USA. ⁷Würzburg-Dresden Cluster of Excellence ct.qmat, TU Dresden, 01062 Dresden, Germany. ✉email: tobias.ritschel@tu-dresden.de; jochen.geck@tu-dresden.de

Novel quantum states and their mutual interactions are a major topic of contemporary condensed matter science. Famous and intensively studied examples are unconventional superconductivity¹, charge-density waves², quantum spin liquids³, topological states of matter⁴, or Dirac materials⁵. Here two branches of research are attracting particularly much attention: The first one is the role of fluctuating electronic order and quantum magnetism for superconductivity¹. The second one, is the combination of topological concepts and superconductivity in the very sought-after topological superconductors⁶.

In this regard, transition metal dichalcogenides (TMDs) of the type TX_2 (T : transition metal, X : chalcogenide) are extremely interesting, as they are, in fact, notorious for harboring a variety of intriguing quantum phenomena. To name just a few cases in point, both superconductivity and charge-density waves occur in $NbSe_2$, $TaSe_2$, and TaS_2 , while WTe_2 presently attracts a lot of interest in the context of topological Weyl-physics^{4,7–9}. Typical TMDs can be regarded as stacks of two-dimensional planes with relatively weak interactions between the planes. As a result, the electronic structure of TMDs is usually very anisotropic and possesses a pronounced two-dimensional character, which, in turn, promotes electronic instabilities and unconventional electronic ground states.

The TMD material $IrTe_2$ is no different in this respect and, indeed, turns out to be an extremely interesting case: In its trigonal $1T$ -structure (Fig. 1a, b), $IrTe_2$ exhibits bulk Dirac points, spin-orbit driven gap inversions and the corresponding topological surface states, which all emerge from the Te $5p$ derived bands^{10–13}. It is particularly exciting that this system not only hosts a topological electronic band structure but also superconductivity below 3 K, raising great hopes for intrinsic topological superconductivity^{14–17}.

Apart from this, there is also electronic order. In fact, various ordered states have been reported, which, referring to the trigonal space group $P\bar{3}m1$ (#164, CdI_2 -structure), can be characterized by wave vectors $\vec{q}_n = (1/(3n+2), 0, 1/(3n+2))$ with $n = 1, 2, \dots, \infty$ where $\vec{q}_\infty = (1/6, 0, 1/6)$ ¹⁸. The orderings can

be constructed from simple basic building blocks containing subunits with very short Ir-Ir distances¹⁸. This Ir-pair is part of a larger (multicenter) object, which is, however, commonly referred to as “dimer” in the literature, although it involves both Te- and Ir-states¹⁹. These dimers form ordered lattices which could be referred to as molecular orbital crystals. In bulk $IrTe_2$ at ambient pressure below 280 K, this lattice of dimers is characterized by $\vec{q}_{n=1} = (1/5, 0, 1/5)$ and it transforms into a lattice with $\vec{q}_{n=2} = (1/8, 0, 1/8)$ upon further cooling at 180 K¹⁸. Different molecular orbital crystals can also coexist in different regions of the sample^{18,20,21}, although it appears that with decreasing temperature T , a larger n becomes stable.

In bulk crystals, the ordering of dimers competes with superconductivity. As soon as this preemptive static order is suppressed, superconductivity can emerge in bulk crystals at low temperatures²². In the case of $IrTe_2$ -nanoflakes that are only a few atomic layers thick, however, the situation has been found to be different. As reported in a very recent study, the superlattice of dimers in these nanoflakes does actually support two-dimensional superconductivity²³. Superconductivity and ordered dimers are, therefore, not just competing but interacting in a more complex manner. One cornerstone for a better understanding of the interplay between dimers, topological electrons, and superconductivity in $IrTe_2$ is therefore an improved understanding of the dimerization process in $IrTe_2$.

So far, various mechanisms have been introduced to explain the formation of dimers in $IrTe_2$, including partial Fermi-surface nesting²², an orbitally induced Peierls effect²⁴, multicenter bonds of Ir and Te¹⁹, the polymerization-depolymerization of Te-bonds¹⁷ as well as electronic instabilities caused by a van-Hove singularity at the Fermi level²⁵. The multitude of scenarios quoted above demonstrates that, despite extensive research efforts, important aspects of dimerization in $IrTe_2$ remain controversial.

To address this issue and to shed light on the physics at work, we performed high-pressure x-ray diffraction studies of pristine $IrTe_2$ single crystals. In this way, we obtain structural information, which we then use for an analysis within density functional

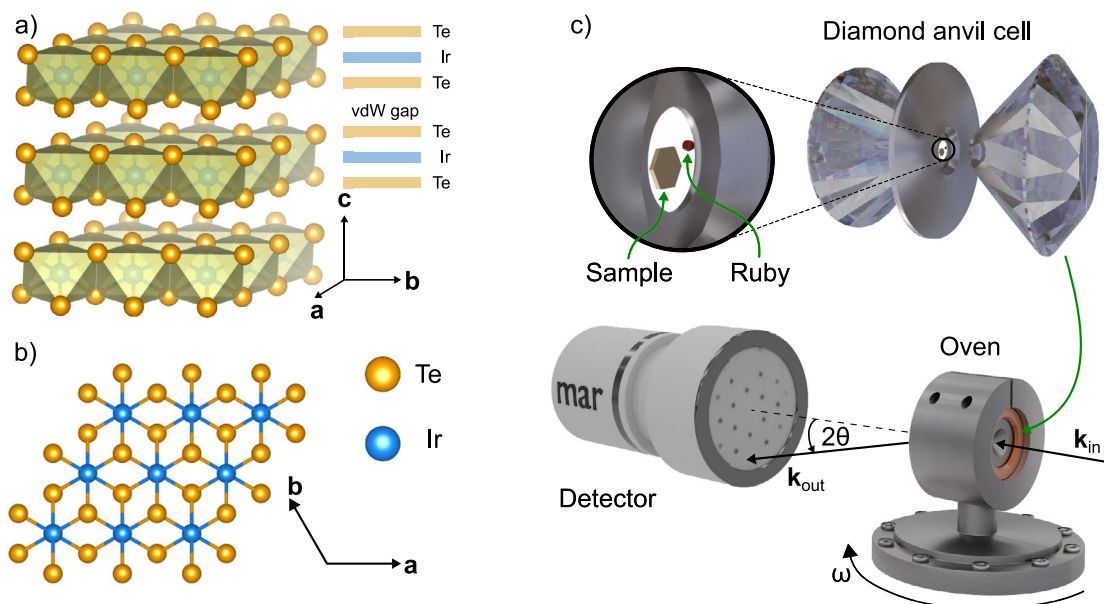


Fig. 1 Host crystal structure of $IrTe_2$ and experimental setup. **a** Side view of the trigonal $1T$ (spacegroup: 164) host crystal structure of $IrTe_2$. The layered structure of $IrTe_2$ with a van der Waals gap in between Te-Ir-Te layers is illustrated on the right. **b** Top view of the host crystal structure of $IrTe_2$ (**a**, **b**, and **c** indicate the lattice vectors). **c** High-pressure x-ray diffraction setup at the beamline ID27 at the European Synchrotron Radiation Facility (ESRF). The sample is placed in a diamond anvil cell mounted in an oven which can be rotated around ω . k_{in} and k_{out} are the wave vectors of the incoming and scattered photons, respectively. 2θ is the scattering angle.

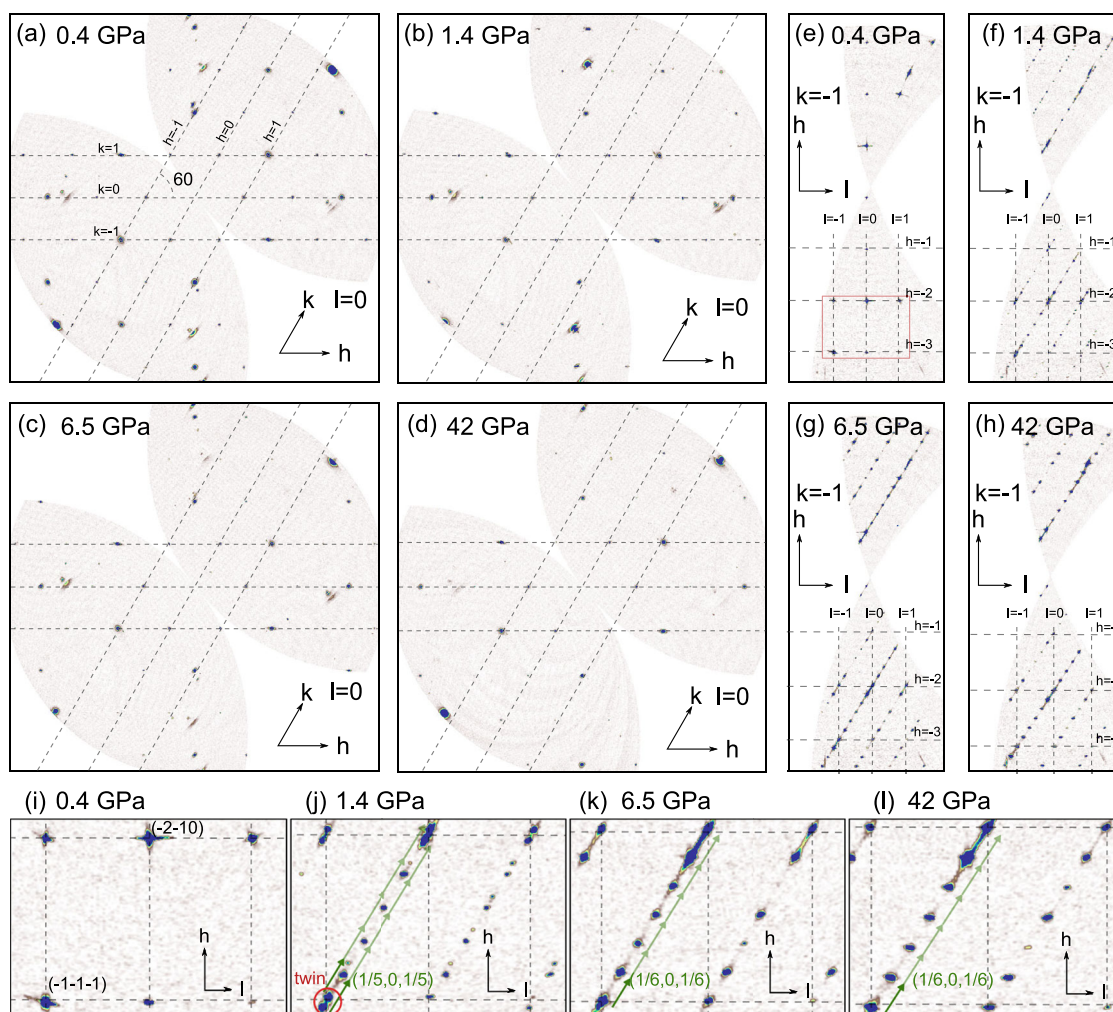


Fig. 2 Reconstructed reciprocal space maps as a function of pressure. **a–d** $hk0$ -planes for the trigonal host phase at 300 K and 0.4 GPa (**a**), the triclinic $1/5$ -phase at 300 K and 1.4 GPa (**b**), the monoclinic $1/6$ -phase at 350 K and 6.5 GPa (**c**), and at 42 GPa (**d**). **e–h** Same as (**a–d**) but for the $h\bar{1}l$ -plane. **i–l** magnifications of the images shown in (**e–h**). The red rectangle in (**b**) indicates the region which is magnified in (**i–l**). Reciprocal lattice vectors and Miller indices h , k , and l refer to the hexagonal cell and an approximately hexagonal cell for the $1/5$ - and $1/6$ -phase. Green arrows in (**j–l**) depict the q -vector.

theory. The key result of this combined study is a change in the Ir-Te-Ir bond angle within the dimers, which is instrumental for their stabilization by the formation of localized multicenter bonding orbitals.

Results

High-pressure x-ray diffraction. Especially, when dealing with competing phases, as is the case here, external pressure is a particularly valuable tool, because it is a clean control parameter that avoids unwanted side effects, which may be caused by local changes induced by chemical substitution or doping. We, therefore, performed high-pressure XRD experiments at pressures P up to 42 GPa and temperatures between room temperature and 420 K (see methods section). The experimental setup is sketched in Fig. 1c.

For each pressure point, one image was collected by continuously recording the diffracted intensity on the detector during a large ω -rotation over $\pm 31^\circ$. These measurements provide a qualitative overview allowing quick detection of structural changes. Hence we will refer to them as overview scans in the following. At selected pressure values, identified using these overview scans, single crystal XRD data sets have been collected. These data sets consist of images integrating over $\Delta\omega = 0.5^\circ$. The

obtained single crystal data has then been used for the crystallographic structure refinements (see methods section). Detailed results of the refinements are given in Supplementary Note 1.

In Fig. 2, we present representative reciprocal space maps of the data at different pressure-temperature points. At small pressures, here, $P = 0.4$ GPa in panels a, b, and i, we observe the trigonal phase ($P\bar{3}m1$) as expected. Figure 2a shows a $(h, k, 0)$ -plane of the reciprocal lattice, while a $(h, -1, l)$ -plane is presented in Fig. 2b, i. The vertices of the dashed lines in the panels indicate the positions of the reciprocal lattice of the trigonal phase, which coincide perfectly with all reflections originating from the sample. The additional spots outside the trigonal grid are all due to the diamond anvils of the DAC.

Upon increasing the pressure to $P = 1.4$ GPa, the diffraction pattern changes drastically, as can be observed in panels b, f, and j of Fig. 2. Most prominently, additional reflections appear in the $(h, -1, l)$ -plane (Fig. 2f, j). The width and intensity of these additional reflections is comparable to that of the Bragg-reflections in the trigonal phase, i.e., we are not dealing with a small lattice modulation as, for example, in a typical weak coupling charge-density wave phase. As can be observed nicely in Fig. 2b) by direct inspection, the Bragg-spots at $P = 1.4$ GPa deviate slightly from the trigonal reciprocal lattice (dashed lines).

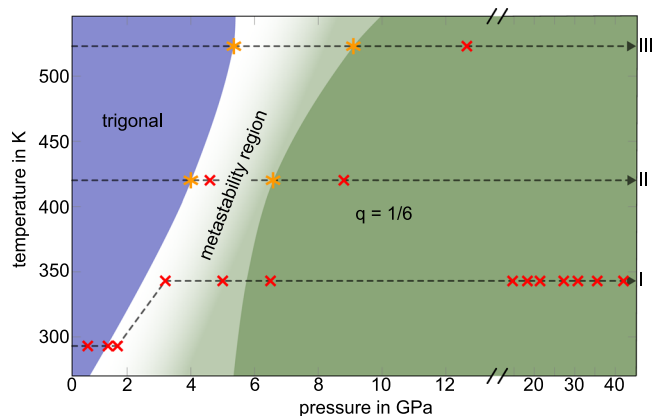


Fig. 3 Pressure-temperature phase diagram of IrTe₂ as deduced from the present x-ray diffraction data. Starting from the trigonal phase without dimers, a metastability region is entered upon increasing pressure. In this region, different ordered phases appear and sometimes coexist. With further increasing pressure, the long-ranged ordered $q = 1/6$ -phase is reached, which remains stable up to 42 GPa. Three samples have been measured at different temperatures as a function of increasing pressure, as indicated by the dashed paths I, II, and III. Red crosses indicate points where full single crystal diffraction data sets have been recorded. Orange stars indicate points where the phase boundary has been observed in an overview scan, i.e., one detector image recorded during a ω -rotation over $\pm 31^\circ$.

In fact, we find a triclinic lattice symmetry under the present conditions ($P\bar{1}$). Nonetheless, still referring to the trigonal low-pressure phase, this new structure can be characterized by the wave vector $\vec{q}_1 = (1/5, 0, 1/5)$, as it is commonly done in the literature. We will refer to this phase as the 1/5-phase in the following. Note that the peak splitting—particularly apparent in Fig. 2j—is not caused by a phase coexistence, but is due to the twinning of the sample under the present conditions. The sample, therefore, shows a pure 1/5-phase, which enabled us to fully refine its structure based on the present data set (see Supplementary Note 1).

Upon increasing P further, the 1/6-phase characterized by $\vec{q}_\infty = (1/6, 0, 1/6)$ is entered. This is shown by the data sets for $P = 6.5$ and 42 GPa presented in Fig. 2. This phase is found to be monoclinic ($C2/c$). The 1/6-phase has been found to remain stable up to the highest pressures. No significant change in the position or width of the detected peaks, other than due to the compression of the lattice, has been observed up to 42 GPa. Interestingly, the probed sample volume in the 1/6-phase was found to be not twinned, as can be observed in Fig. 2k. A possible reason for this detwinning is a small pressure gradient within the DAC. Also, the intensities of the 1/6-phase could be refined successfully, yielding a full determination of this phase (see Supplementary Note 1).

The measurements of our HP-XRD experiments are summarized in the PT phase diagram displayed in Fig. 3. In the region between the trigonal and the 1/6-phase, we observed the 1/5-, 1/8- and the 1/11-phase ($n = 1, 2$, and 3) as well as a coexistence of some of these. For this reason, it is denoted as a “metastability region”.

Our refined 1/5- and 1/6-structures at $p < 6.5$ GPa resemble very closely the corresponding structures found in Se-substituted IrTe₂ at ambient pressure^{18,26}, where the concentration of dimers increases with n : for the 1/5-phase ($n = 1$) the fraction of dimerized Ir is 2/5, for the 1/8-phase ($n = 2$) it is already 1/2, and for the 1/6 ($n = \infty$) it becomes 2/3.

The evolution of the lattice structure with increasing P up to 42 GPa is illustrated in Fig. 4. As described above, the dimerized

phases are no longer trigonal but mono- or triclinic. However, in order to facilitate the comparison among the different phases, these lower symmetry structures have been mapped onto an approximate trigonal cell. Selected structural parameters obtained by this mapping are shown in Fig. 4. While in the truly trigonal phase $a = b$, for the structures of the dimerized phase, only $a \approx b$ is fulfilled. This can be observed in Fig. 4b), where a and b split up upon entering the dimerized phases with increasing P . Panel b and the c/a -ratio in panel d show that, as expected, the c -axis is much more compressible than the a - and b -axis. More specifically, we obtain $4.7 \times 10^{-3} \text{ GPa}^{-1} \approx \kappa_c > \kappa_{a,b} \approx 1.3 \times 10^{-3} \text{ GPa}^{-1}$ for the axial compressibilities. At 42 GPa the c -axis and the unit cell volume are reduced by about 12% and 25%, respectively.

In the trigonal phase, each Ir-site has six nearest neighbor Ir-sites at the same distance $d \approx 3.92 \text{ \AA}$ within the IrTe₂-layer. In the dimerized phases, this changes, and every Ir in a dimer has one short intra-dimer distance d_s and five longer nearest neighbor distances of average length d_l . The formation of the dimers can therefore be tracked very nicely by the ratio $\gamma = d_l/d_s$, which is presented in Fig. 4c). With increasing P , this ratio jumps from $\gamma = 1$ in the trigonal phase (no dimers, $d = d_s = d_l$) to $\gamma \approx 1.27$ ($d_s \approx 3.11 \text{ \AA}$, $d_l \approx 3.96 \text{ \AA}$) in the 1/5-phase. Since γ can be interpreted as an order parameter of the local dimerization, its large value implies a very strong dimerization in IrTe₂. Furthermore, the monotonous increase of γ with P shows that the dimers are more and more stabilized upon pressurization.

A key result of the present refinements concerns the Ir-Te-Ir bond angle α (Fig. 4a): Across the P -driven transition into the 1/5-phase, the angle α inside the dimers collapses from 95.8° to 73.0° , as shown in Fig. 4e. Note, the evolution of α with further increasing P is smooth and monotonous also across the transition into the 1/6-phase. The reduced value of α is not significantly influenced by the specific long-range order, but rather appears to be a characteristic property of the local dimers.

Compared to α , the nearest neighbor Ir-Te distances change much more moderately: The single Ir-Te distance of 2.645 \AA in the trigonal phase splits up upon entering the dimerized phases (see Supplementary Fig. 1). This splitting is of the order of $\pm 0.06 \text{ \AA}$, which amounts to about only 2% of 2.645 \AA . Also, note that the Ir-Te distances of dimerized and non-dimerized Ir-sites exhibit a very similar rate of compression upon increasing P .

The above analysis identifies the Ir-Te-Ir bond angle α as a key structural parameter for dimerization. α essentially combines the pronounced reduction of the Ir-Ir distance at almost constant Ir-Te distances into a single parameter. The question now obviously is, which role α plays in the stabilization of dimers in IrTe₂.

Density functional theory. To address precisely this question and to elucidate the relation between the formation of dimers and the electronic structure, we performed density functional theory (DFT) calculations based on the experimentally determined lattice structures. Calculations for four different structures were performed, namely (i) the trigonal structure, (ii) the pure 1/5-phase, (iii) the 1/6-phase at 6.5 GPa, and (iv) the 1/6-phase at 42 GPa (structural parameters are given in Supplementary Tables III, IV). The electronic bands obtained for the 1/5- and 1/6-phase have been unfolded onto the original Brillouin zone of the trigonal structure, using the approach described by ref. 27. In this way, the electronic bands for the three different structures can be compared directly.

We first discuss the evolution of the bulk DFT band structure with increasing hydrostatic pressure. As described very nicely by ref. 10, the chalcogenide p-orbital manifold is the most important one for the formation of Dirac cones, topological surface states,

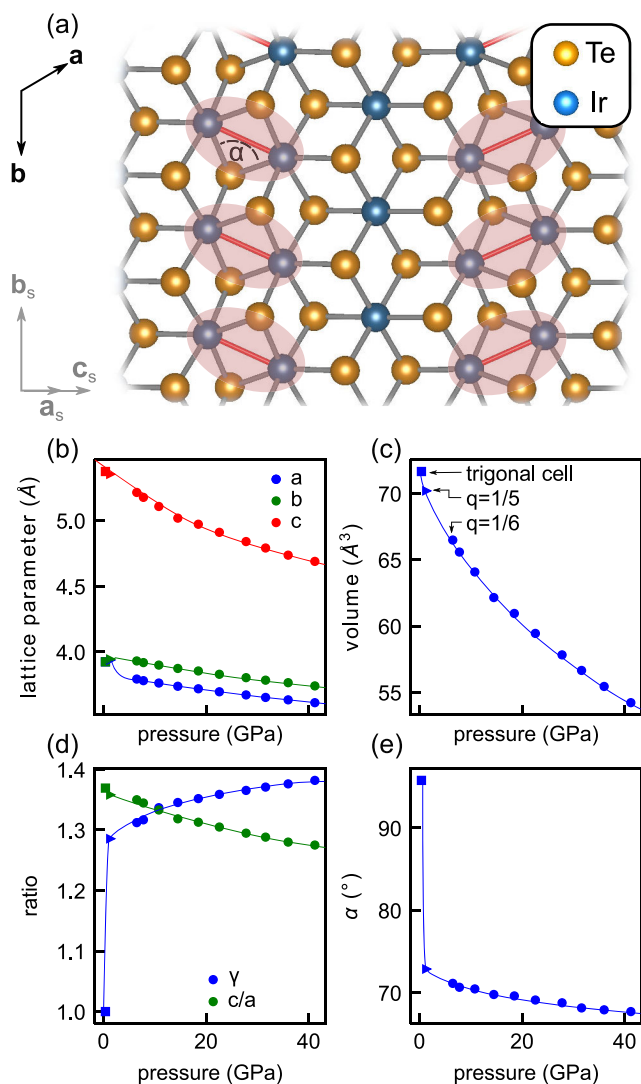


Fig. 4 Structural parameters as determined from the single crystal data as a function of pressure. **a** Sketch of one Te-Ir-Te layer in the $q=1/6$ structure. The short Ir-Ir distances inside the dimers are highlighted in red. All parameters in **(b–e)** are derived from a transformation of the supercell back to an approximately trigonal cell. The corresponding (pseudo)-trigonal in-plane lattice vectors \mathbf{a} and \mathbf{b} are indicated as black arrows. The lattice vectors corresponding to the monoclinic $q=1/6$ structure (\mathbf{a}_s , \mathbf{b}_s and \mathbf{c}_s) are shown in gray. Note that the in-plane directions in terms of the monoclinic cell are given by $\mathbf{a}_s + \mathbf{c}_s$ and \mathbf{b}_s . **b, c** The (pseudo)-trigonal lattice parameters and cell volume as a function of pressure. **d** c/a -ratio (green) and the ratio between long and short Ir-Ir bonds $\gamma = d_l/d_s$ (blue). **e** Ir-Te-Ir angle α as indicated in **(a)**. Error bars in **(b–e)** are smaller than the symbol size. Square, triangular and circular symbols correspond to data from the trigonal, triclinic $q=1/5$ - and monoclinic $q=1/6$ -phase. Solid lines are guides to the eye.

and topological surface resonances. In Fig. 5a–d, we, therefore, show so-called fat bands in which the Te $5p_{x,y,z}$ -character is represented by the line thickness and the color.

The results for the trigonal phase in Fig. 5a agree very well with previously published DFT- and ARPES-results²⁵, including the van-Hove singularity at the Fermi level along the AL -direction (indicated by a black arrow in Fig. 5a). Our DFT band structure, also exhibits precisely the features that have been discussed by ref. ¹⁰ Firstly, there is a type II bulk Dirac point (BDP) along the ΓA -direction, which is protected by the C_{3v} -symmetry of the

lattice. More to the point, the C_{3v} -symmetry forbids hybridization of Te $5p_{x,y}$ and $5p_z$ bands along the ΓA -direction so that there is no hybridization gap. The two bands, therefore, cross at the BDP, forming states that correspond to massless Dirac-fermions. In the present case, however, the BDP is above the Fermi level. Secondly, inverted band gaps of the bulk electronic structure are obtained as well. These inverted band gaps are expected to result in topological surface states and resonances¹⁰, which indeed appears to be consistent with a very recent ARPES-study¹¹.

Using the structural refinements described above as input for DFT, we can now address the evolution of the electronic structure with increasing hydrostatic pressure. As is obvious from Fig. 5b–d, the pressure-induced appearance of dimers causes drastic changes in the electronic band structure: Starting from the triclinic $1/5$ -phase, a strong splitting of the bands is apparent with states entering the energy regions of the inverted band gaps. The band crossing of the BDP is lost and a gap opens, which corresponds to the formation of massive Dirac states, due to the broken C_{3v} -symmetry. Upon increasing the applied pressure further, the monoclinic $1/6$ -phase occurs. In this phase, the band gap at the former BDP opens up further.

By comparing the energies of the $5p_z$ -states at Γ and A , one can see that the energy spread of these states increases with increasing pressure, as expected from the reduced c/a -ratio. But also, the $5p_{xy}$ -type bands change strongly. In particular, we also find that the van-Hove singularity along the AL -direction, indicated with black arrows in Fig. 5a–d, is pushed further below the Fermi level in agreement with previous studies²⁵.

Along the ΓL -direction, which is parallel to the wave vectors of the ordered dimers, a gap opens between the occupied and the unoccupied states (Fig. 5g) This agrees perfectly with the earlier conclusion that—in direct space—the electrons become confined to the two-dimensional layers between neighboring dimer-walls^{18,23}.

Figure 5f shows the evolution of the density of states (DOS) with pressure. Also, here the drastic changes in the electronic structure can clearly be discerned. Indeed, the changes caused by applying P correspond closely to what has been found for the $1/5$ -phase at ambient pressure but lower temperature¹⁹. Most important for the following discussion are the bonding states formed by Te $5p$ and Ir $5d$ that are pushed out of the broad band-continuum between 0 and -6 eV, once the dimers form (indicated by the green arrow in Fig. 5f). Using the results from our XRD measurements, we can now follow the evolution of these bonding dimer-states with increasing P . As can be observed in Fig. 5f, these bonding dimer-states shift very strongly to lower and lower energies, with P growing from 1.4 to 41 GPa. Indeed there is a huge shift of about 2 eV, which amounts to a relative change of $\sim 30\%$.

The energy-resolved charge distribution corresponding to these bonding dimer-states is illustrated in Fig. 6. As before, the short Ir-Ir distances within the dimers in panel a are indicated by red lines. Inspection of Fig. 6a reveals a ring-shaped charge-density distribution going around every short Ir-Ir link (gray-colored charge clouds which correspond to a level of $6 \times 10^{-4} e/\text{Å}^{-3}$). This can be also seen in the cuts through the charge density along planes i and ii in Fig. 6a. The same contour plots are also shown in more detail in Fig. 6b and c. Note the strong distortion of the angle α of the Ir-Te-Ir links that is clearly apparent in Fig. 6a, b.

The most bonding states of the dimer are, therefore, not due to direct Ir-Ir interactions. A detailed analysis of the chemical bonds in IrTe_2 indeed showed that direct Ir-Ir bonding is not relevant¹⁹. Instead, we find that the ring-shaped multicenter covalent bond, which is formed by Ir $5d$ and Te $5p$ states, plays a key role in the stabilization of the dimers. This is verified by the strong P -driven stabilization of this bond, which goes hand in hand with the experimentally observed change in α .

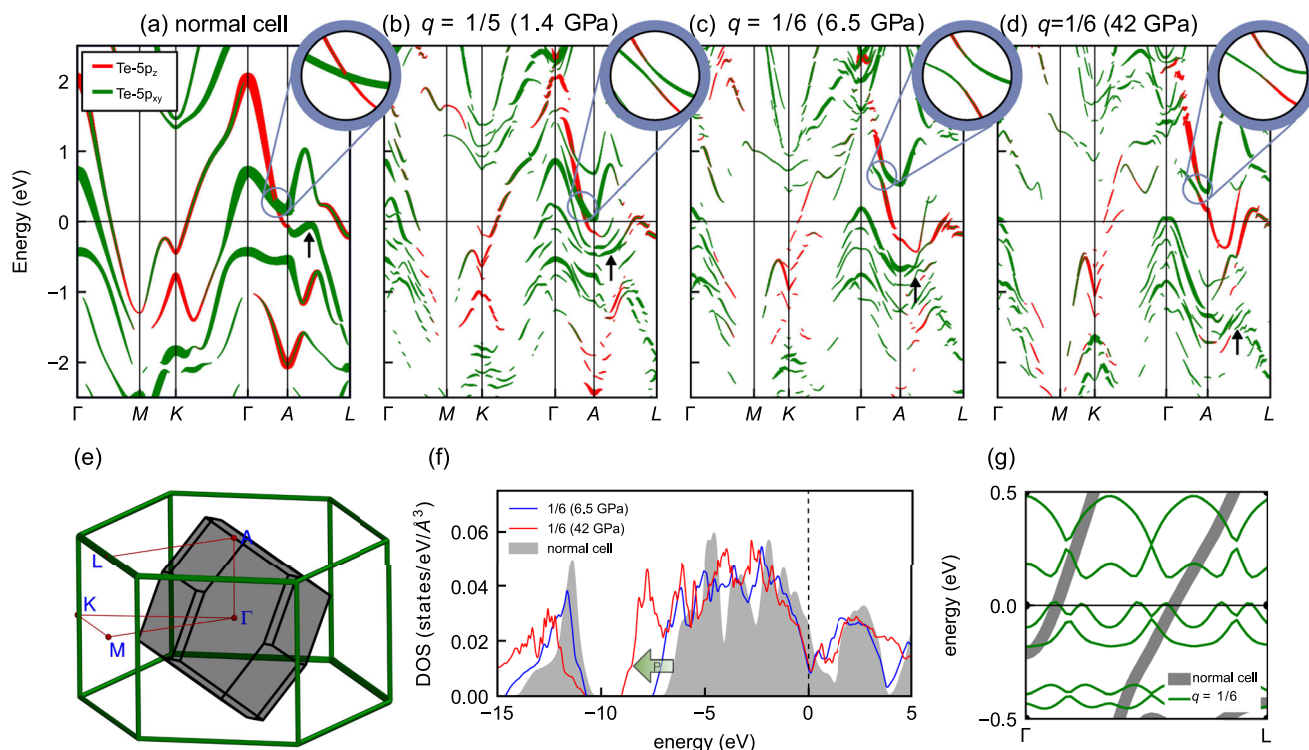


Fig. 5 Electronic structure as a function of hydrostatic pressure. **a–d** Fat bands representing the Te-5p character for the trigonal structure at ambient conditions **(a)**, the $q = 1/5$ structure **(b)**, and the $q = 1/6$ structure **(c, d)**. Band weights of the $q = 1/5$ and $q = 1/6$ -phase were unfolded into the Brillouin zone of the trigonal structure. A magnification of the regions around the bulk Dirac point is shown in the insets. **e** The trigonal Brillouin zone (BZ) is depicted by green lines and the BZ of the monoclinic 1/6-phase by black lines and gray surfaces. All high-symmetry points refer to the trigonal BZ. **f** Total density of states (DOS) at ambient conditions (trigonal cell) and for the $q = 1/6$ -phase at 6.5 GPa and 42 GPa. The green arrow indicates the shift of the dimer bonding states to lower energies with increasing pressure. **g** Comparison of the band structure along the q -direction of the 1/6-phase with the trigonal cell band structure.

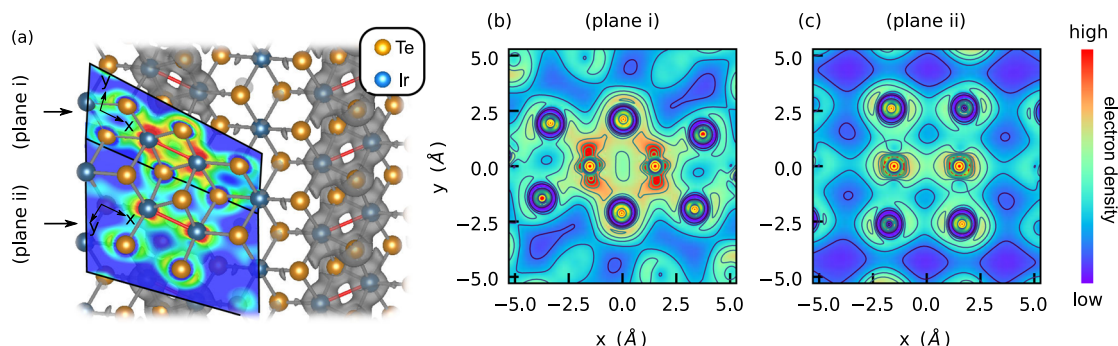


Fig. 6 Charge-density distribution of the bonding dimer-states in the 1/6-phase. The shown electron density corresponds to the Kohn-Sham states within an energy window of -7 to -6.5 eV for a density functional theory calculation which uses the experimental crystal structure at 6.5 GPa. **a** Cuts through the charge density parallel to two different planes (i, ii) placed into the lattice structure. The short Ir-Ir distances within a dimer are indicated by red lines. Gray-shaded ring-like structures indicate the charge distribution of the bonding states of the dimers (contour level of the iso surface: 6×10^{-4} e/Å⁻³). **b, c** Contour plots of the charge densities of these covalent bonds for plane i and plane ii. The position of the planes is indicated in **(a)**. The color bar quantifies the electron density.

Discussion

The important role of the ring-shaped multicenter covalent bonds for the dimers has also been found by ref. ¹⁹. The key new result of the present study concerns the stabilization of these bonds: Our XRD data reveals that the bond angle α changes drastically with pressure, while the Ir-Te distances change only slightly and continuously across the phase transitions. At the same time, our DFT results show that with increasing P , the binding energy of the localized multicenter bonds is pushed further below the broad band-continuum formed by itinerant Ir 5d and Te 5p

states. The very large energy shifts of up to 2 eV cannot be explained by the small changes of the Ir-Te bond lengths, which, furthermore, change by essentially the same amount for Ir-sites within and outside a dimer. We, therefore, conclude that α is the relevant structural degree of freedom for the stabilization of the ring-shaped multicenter bond, which connects two edge-sharing IrTe₆-octahedra and is formed by Te 5p- and Ir 5d-states.

One way to rationalize this, is to consider two molecular orbitals involving Ir(5d- e_g) and Te(5p) states on each of the two edge-sharing IrTe₆-octahedra of a dimer (Fig. 7). In the edge-

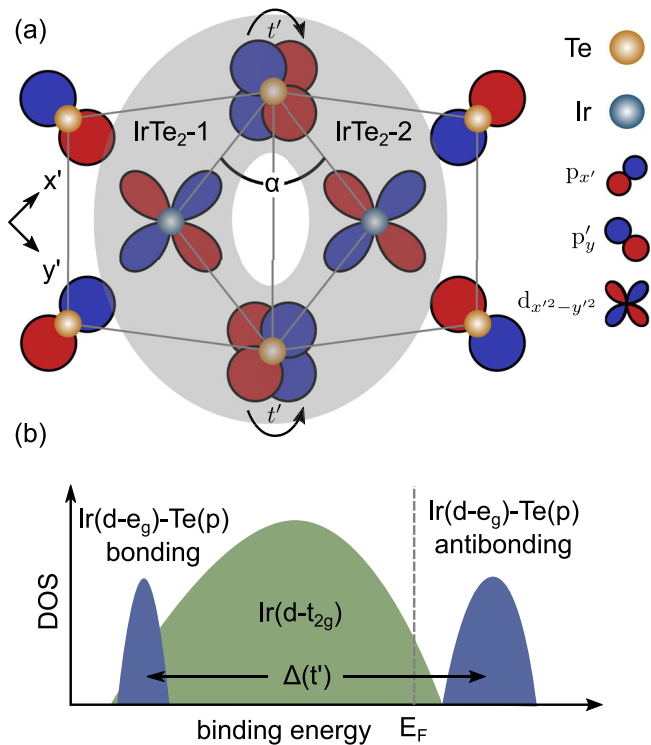


Fig. 7 Schematic illustration of the bonding mechanism. **a** Bonding geometry between the two edge-sharing IrTe_6 -octahedra (IrTe_6 -1 and IrTe_6 -2) forming the dimer. As α deviates from 90° , the overlap t' between the Te- p orbitals on the shared Te-sites increases and a 4-center bonding orbital can form (light gray ring). **b** The overlap t' determines the energy splitting between bonding and anti-bonding states. Note, the coordinate system in **(a)** x', y' is rotated by 45° with respect to the coordinate system shown in Fig. 6 (plane i).

sharing geometry, the overlap of these two molecular orbitals is governed by the overlap t' of the involved Te($5p$) orbitals on the shared Te-sites which changes very strongly with α . More specifically, the overlap t' increases rapidly as α deviates from 90° . As a result, the energy splitting of the derived bonding-anti-bonding states increases as t' grows. Accordingly, the observed reduction of α towards 70° with increasing P yields a strong stabilization of the multicenter bond between the two IrTe_6 -octahedra. There are two key features of this mechanism: First, it is essentially local, since it corresponds to the formation of a local multicenter bond linking two edge-sharing IrTe_6 -octahedra. Importantly, this multicenter bond is not stabilized by direct Ir-Ir interactions, which is very surprising considering the strong shortening of the Ir-Ir distance within a dimer. Second, the strong change of the electronic binding energy with α implies a very strong coupling of the corresponding electrons with the lattice.

The mechanism identified in this study is different from other mechanisms discussed previously, especially those referring to weak coupling scenarios based on the electronic band structure. Such scenarios are not easily reconciled with the various \vec{q}_n observed experimentally, because they involve specific wave vectors defined by the band structure of the trigonal phase. The local α -dependent hybridization, however, is not tied to details of the band structure, i.e., it can easily accommodate the different and often coexisting \vec{q}_n found in experiment. We emphasize that the specific type of long-range order under certain conditions, i.e. the specific \vec{q}_n , may very well be determined by the underlying electronic band structure. According to our analysis, however, the

primary stabilization mechanism of the dimers is the local α -dependent hybridization between neighboring IrTe_6 -octahedra.

The formation of localized multicenter bonds will compete against the delocalization of charges in band-like states. In other words, the local stabilization mechanism must be strong enough to pull the bonding states out of the broad band-continuum. According to DFT, this is indeed the case here. Nonetheless, this competition may explain why so far, no phase, in which all Ir-sites are part of a multicenter bond—or a dimer, for that matter—have been observed, and all electronic crystals composed of multicenter bonding orbitals still feature mobile charge carriers.

We also note that the multicenter bond formation described here does not involve charge order in the sense of Ir-sites with significantly different valences. In the present multi-site situation with extended Ir- and Te-states it is hardly possible to assign a certain charge to a specific lattice site. In addition, we are dealing with very similar electron affinities of Ir and Te. A charge ordering scenario, therefore, appears to be inadequate. Notwithstanding, the electronically ordered phases, of course, possess nonequivalent Ir-sites, which, for instance, explain the peak splittings observed in x-ray photoemission spectroscopy¹¹—even without different valences of Ir.

The formation of the multicenter bonds involves changes in the occupied Te- and Ir-states, which is at least qualitatively consistent with the depolymerization scenarios discussed earlier¹⁷. Referring to this scenario, our analysis provides a mechanism underlying the depolymerization: The formation of strong intra-layer multicenter bonds on neighboring edge-sharing IrTe_6 -octahedra results in a weakening of the inter-layer Te-Te bonds.

Since the stabilizing mechanism of the multicenter bonds is essentially local, it does not depend on details of the band structure and should be weakly dependent on doping. This mechanism can therefore be expected to be active in doped IrTe_2 as well. It is hence very interesting to ask whether local and possibly dynamic multicenter bonds also exist in the trigonal phases and whether they could play a role in the superconductivity in doped IrTe_2 . Going beyond the specific case of IrTe_2 , it will now also be important to investigate the relevance of this mechanism in other materials featuring extended p and d valence states, especially with regard to magnetic instabilities, topology, and superconducting states. These questions certainly deserve to be scrutinized in future studies.

Methods

High-pressure X-ray diffraction. The high-pressure XRD measurements have been performed at the beamline ID27 of the European Synchrotron Radiation Facility (ESRF) in Grenoble, using a monochromatic beam with a photon energy of 33 keV ($\lambda = 0.3738 \text{ \AA}$) and a spot size of $3 \times 3 \mu\text{m}$. High-quality single crystals have been loaded into a membrane-driven diamond anvil cell (DAC) with helium as a pressure transmitting medium. The pressure inside the DAC has been monitored in situ using the $R_{1,2}$ fluorescence of Cr-centers in a ruby sphere close to the sample. For the present temperature-dependent measurements between room temperature and 420 K, the DAC has been installed in an oven, which was itself mounted on a single axis (ω) goniometer that has been equipped with a MARCCD area detector for efficient detection of the diffracted intensities.

X-ray data analysis and structure refinement. All data processing was performed in the CrysAlisPro software suite (version 171.39.46)²⁸. Empirical absorption correction was applied using spherical harmonics, implemented in the SCALE3 ABSPACK scaling algorithm. The subsequent structure solution and weighted full-matrix least-squares refinement on F^2 were done with SHELXT-2014/5²⁹ and SHELXL-2018/3³⁰ as implemented in the WinGx 2018.3 program suite³¹. As reciprocal space coverage is significantly reduced by the DAC, the crystal structures were exclusively refined with isotropic displacement parameters. The ratio of independent reflections to refined parameters exceeds a value of ten for all data sets, with the exception of the data set for the trigonal phase measured at $P = 0.4 \text{ GPa}$. The parameters of the data collection and the results of the structural refinement are summarized in Supplementary Tables I and II. The atomic positions and isotropic displacement parameters are listed in Supplementary Tables III and IV and CIF files are supplied in Supplementary Data File 1.

Density functional theory. The first-principle calculations have been done using the FPLO package (version 18)³². We used the local density approximation (LDA) and the generalized gradient approximation (GGA) of the exchange-correlation potential^{33,34}. We found very little differences in the resulting band structure for the two approximations. Therefore, we present the results from the calculations performed within LDA. In order to account for spin-orbit coupling, the calculations were performed within the full four-component Dirac-Kohn-Sham theory as implemented in FPLO³⁵. The total density was converged on a grid of $24 \times 24 \times 24$ and $12 \times 12 \times 12$ irreducible k-points for the normal cell and the supercell calculations, respectively. Brillouin zone integration was done using the tetrahedron method. All calculations were performed using the experimentally determined structure.

Data availability

Crystallographic information files (CIFs) are available in Supplementary Data File 1. All other data that support the findings of this study are available from the corresponding authors upon reasonable request.

Received: 20 November 2021; Accepted: 18 November 2022;

Published online: 12 December 2022

References

- Stewart, G. R. Unconventional superconductivity. *Adv. Phys.* **66**, 75–196 (2017).
- Arpaia, R. et al. Dynamical charge density fluctuations pervading the phase diagram of a Cu-based high-T_c superconductor. *Science* **365**, 906–910 (2019).
- Savary, L. & Balents, L. Quantum spin liquids: a review. *Rep. Progr. Phys.* **80**, 016502 (2017).
- Yan, B. & Felser, C. Topological materials: Weyl semimetals. *Annu Rev. Condens. Matter Phys.* **8**, 337–354 (2017).
- Wehling, T. O., Black-Schaffer, A. M. & Balatsky, A. V. Dirac materials. *Adv. Phys.* **63**, 1–76 (2014).
- Sato, M. & Ando, Y. Topological superconductors: a review. *Rep. Progr. Phys.* **80**, 076501 (2017).
- Rossnagel, K. On the origin of charge-density waves in select layered transition-metal dichalcogenides. *J. Phys. Condens. Matter* **23**, 213001 (2011).
- Yang, H., Kim, S. W., Chhowalla, M. & Lee, Y. H. Structural and quantum-state phase transitions in van der Waals layered materials. *Nat. Phys.* **13**, 931–937 (2017).
- Gye, G., Oh, E. & Yeom, H. W. Topological landscape of competing charge density waves in 2H-NbSe₂. *Phys. Rev. Lett.* **122**, 016403 (2019).
- Bahramy, M. S. et al. Ubiquitous formation of bulk Dirac cones and topological surface states from a single orbital manifold in transition-metal dichalcogenides. *Nat. Mater.* **17**, 21–28 (2018).
- Nicholson, C. W. et al. Uniaxial strain-induced phase transition in the 2d topological semimetal IrTe₂. *Commun. Mater.* **2**, 25 (2021).
- Fei, F. et al. Band structure perfection and superconductivity in type-II Dirac semimetal Ir_{1-x}Pt_xTe₂. *Adv. Mater.* **30**, 1801556 (2018).
- Jiang, J. et al. A comprehensive ARPES study on the type-II Dirac semimetal candidate Ir_{1-x}Pt_xTe₂. *APL Mater.* **8**, 061106 (2020).
- Kiswandhi, A. et al. Competition between the structural phase transition and superconductivity in Ir_{1-x}Pt_xTe₂ as revealed by pressure effects. *Phys. Rev. B* **87**, 121107 (2013).
- Kudo, K., Kobayashi, M., Pyon, S. & Nohara, M. Suppression of structural phase transition in IrTe₂ by isovalent Rh doping. *J. Phys. Soc. Jpn.* **82**, 085001 (2013).
- Kamitani, M. et al. Superconductivity in Cu_xIrTe₂ driven by interlayer hybridization. *Phys. Rev. B* **87**, 180501 (2013).
- Oh, Y. S., Yang, J. J., Horibe, Y. & Cheong, S.-W. Anionic depolymerization transition in IrTe₂. *Phys. Rev. Lett.* **110**, 127209 (2013).
- Pascut, G. L. et al. Series of alternating states with unpolarized and spin-polarized bands in dimerized IrTe₂. *Phys. Rev. B* **90**, 195122 (2014).
- Saleh, G. & Artyukhin, S. First-principles theory of phase transitions in IrTe₂. *J. Phys. Chem. Lett.* **11**, 2127–2132 (2020). PMID: 32079398.
- Hsu, P.-J. et al. Hysteretic melting transition of a soliton lattice in a commensurate charge modulation. *Phys. Rev. Lett.* **111**, 266401 (2013).
- Chen, C. et al. Surface phases of the transition-metal dichalcogenide IrTe₂. *Phys. Rev. B* **95**, 094118 (2017).
- Yang, J. et al. Charge-orbital density wave and superconductivity in the strong spin-orbit coupled IrTe₂/Pd. *Phys. Rev. Lett.* **108**, 116402 (2012).
- Park, S. et al. Superconductivity emerging from a stripe charge order in IrTe₂ nanoflakes. *Nat. Commun.* **12**, 3157 (2021).
- Ootsuki, D. et al. Orbital degeneracy and Peierls instability in the triangular-lattice superconductor Ir_{1-x}Pt_xTe₂. *Phys. Rev. B* **86**, 014519 (2012).
- Qian, T. et al. Structural phase transition associated with van Hove singularity in 5d transition metal compound IrTe₂. *N. J. Phys.* **16**, 123038 (2014).
- Pascut, G. L. et al. Dimerization-induced cross-layer quasi-two-dimensionality in metallic IrTe₂. *Phys. Rev. Lett.* **112**, 086402 (2014).
- Ku, W., Berlijn, T. & Lee, C.-C. Unfolding first-principles band structures. *Phys. Rev. Lett.* **104**, 216401 (2010).
- Rigaku Oxford Diffraction. CrysAlisPro software system version 1.171.39.46 (Rigaku Corporation, 2018).
- Sheldrick, G. M. SHELXT—integrated space-group and crystal-structure determination. *Acta Crystallogr. Sect. A Found. Adv.* **71**, 3–8 (2015).
- Sheldrick, G. M. Crystal structure refinement with SHELXL. *Acta Crystallogr. Sect. C. Struct. Chem.* **71**, 3–8 (2015).
- Farrugia, L. J. WinGX and ORTEP for windows: an update. *J. Appl. Crystallogr.* **45**, 849–854 (2012).
- Koepnick, K. & Eschrig, H. Full-potential nonorthogonal local-orbital minimum-basis band-structure scheme. *Phys. Rev. B* **59**, 1743–1757 (1999).
- Perdew, J. P. & Wang, Y. Accurate and simple analytic representation of the electron-gas correlation energy. *Phys. Rev. B* **45**, 13244–13249 (1992).
- Perdew, J. P., Burke, K. & Ernzerhof, M. Generalized gradient approximation made simple. *Phys. Rev. Lett.* **77**, 3865–3868 (1996).
- Eschrig, H., Richter, M. & Ophale, I. In *Relativistic Electronic Structure Theory, Part 2. Applications* Vol. 13 (ed. Schwerdtfeger, P.) Ch. 12 (Elsevier, 2004).

Acknowledgements

This research has been supported by the Deutsche Forschungsgemeinschaft through projects C06 and C09 of the SFB 1143 (project-id 247310070) and the Würzburg-Dresden Cluster of Excellence on Complexity and Topology in Quantum Matter-ct.qmat (EXC 2147, project-id 390858490). The work at Rutgers University was supported by the DOE under Grant No. DOE-DE-FG02-07ER46382.

Author contributions

S.-W.C. and J.G. conceived the high-pressure diffraction experiment. S.-W.C. and J.Y. provided IrTe₂ single crystals. T.R., J.T., M.K., G.G., V.S., M.M., and J.G. conducted the diffraction experiment at the ESRF. T.R., Q.S., M.K., and J.G. analyzed the diffraction data and T.R. performed the DFT study. The manuscript has been written with contributions from all authors.

Funding

Open Access funding enabled and organized by Projekt DEAL.

Competing interests

The authors declare no competing interests.

Additional information

Supplementary information The online version contains supplementary material available at <https://doi.org/10.1038/s42005-022-01094-9>.

Correspondence and requests for materials should be addressed to Tobias Ritschel or J. Geck.

Peer review information *Communications Physics* thanks the anonymous reviewers for their contribution to the peer review of this work. Peer reviewer reports are available.

Reprints and permission information is available at <http://www.nature.com/reprints>

Publisher's note Springer Nature remains neutral with regard to jurisdictional claims in published maps and institutional affiliations.



Open Access This article is licensed under a Creative Commons Attribution 4.0 International License, which permits use, sharing, adaptation, distribution and reproduction in any medium or format, as long as you give appropriate credit to the original author(s) and the source, provide a link to the Creative Commons license, and indicate if changes were made. The images or other third party material in this article are included in the article's Creative Commons license, unless indicated otherwise in a credit line to the material. If material is not included in the article's Creative Commons license and your intended use is not permitted by statutory regulation or exceeds the permitted use, you will need to obtain permission directly from the copyright holder. To view a copy of this license, visit <http://creativecommons.org/licenses/by/4.0/>.

© The Author(s) 2022